

Study of CeI₃ evaporation in the presence of group 13 metal-iodides

J. J. Curry, E. G. Estupiñán, W. P. Lapatovich, A. Henins, S. D. Shastri, J. E. Hardis, and J. M. Gibbs

Citation: *Journal of Applied Physics* **115**, 034509 (2014); doi: 10.1063/1.4862041

View online: <http://dx.doi.org/10.1063/1.4862041>

View Table of Contents: <http://scitation.aip.org/content/aip/journal/jap/115/3?ver=pdfcov>

Published by the [AIP Publishing](#)



Goodfellow

metals • ceramics • polymers
composites • compounds • glasses

Save 5% • Buy online
70,000 products • Fast shipping

Study of CeI₃ evaporation in the presence of group 13 metal-iodides

J. J. Curry,^{1,a)} E. G. Estupiñán,² W. P. Lapatovich,^{1,b)} A. Henins,^{1,c)} S. D. Shastri,³
 J. E. Hardis,¹ and J. M. Gibbs²

¹National Institute of Standards and Technology, 100 Bureau Drive, Gaithersburg, Maryland 20899, USA

²OSRAM SYLVANIA Inc., 71 Cherry Hill Drive, Beverly, Massachusetts 01915, USA

³Advanced Photon Source, Argonne National Laboratory, 9700 South Cass Avenue, Argonne, Illinois 60439, USA

(Received 29 November 2013; accepted 29 December 2013; published online 17 January 2014)

The influences of GaI₃, InI, and TlI on the evaporation characteristics of CeI₃ have been studied over the temperature range 900 K to 1400 K using x-ray induced fluorescence. The total vapor densities, summed over all atomic and molecular species, of Ce, I, In, and Tl were obtained. Measurements of Ce were limited to temperatures above 1033 K, the melting temperature of CeI₃. This is the highest temperature range for which measurements of the vapor pressure of CeI₃ have been made. The vapor pressure of the CeI₃ monomer above the pure CeI₃ salt for temperatures exceeding its melting point can be approximated by $\log_{10} p/\text{Pa} = 11.24(\pm 0.03) - 10,690(\pm 40)(T/\text{K})^{-1}$ where the numbers in parentheses are standard uncertainties. InI and TlI were shown to modestly enhance the presence of Ce in the vapor phase, up to a factor of 5. GaI₃ produced no enhancement in this temperature range. Numerical simulations of the thermochemical equilibrium suggest the importance of both liquid-phase and vapor-phase complexes. Significant improvement to the method of absolute calibration is discussed. [<http://dx.doi.org/10.1063/1.4862041>]

I. INTRODUCTION

The evaporation characteristics of metal-iodides are a major factor in the performance of metal-halide high-intensity discharge (HID) lamps. The high luminous efficacy and excellent color-rendering of these general-purpose light sources are attributable to the rich visible emission spectra of the free atoms and singly-charged ions of a number of metals. Since the pure metals do not readily evaporate, they are introduced into the lamp in the form of metal-iodides, which have significantly higher vapor pressures. Heat from the lamp discharge raises the temperature of the coldest spot in the lamp to 900 K and higher, sufficient to produce significant vapor pressures of the metal-iodides. Once evaporated, the metal-iodide molecules diffuse or convect into hotter regions of the discharge where they are dissociated to varying degrees. Temperatures in the core of the discharge (4000 K to 7000 K) are high enough to completely dissociate the iodide molecules (MI_x) and to excite the free metal atoms (M) and their ions (M⁺) by electron impact. The number densities of the metal atoms and ions link the performance characteristics of the lamp with the evaporation characteristics of the metal-iodides.

Typically, a lamp contains several different metal-iodides to achieve optimum performance. The number of metal atoms in the discharge is then a function, not only of the pure metal-iodide vapor pressures, but also of the interactions between the various metal-iodides in both the vapor and condensed phases. In particular, simple complexing



between two metal-iodides (M1)I_x and (M2)I_y can be important. In some cases, the hetero-complex (M1)(M2)I_{x+y} can be a much more effective way of getting one of the metals (M1) into the vapor. The complex is then readily dissociated in hotter regions of the discharge. A minimum requirement for this kind of evaporation enhancement is that the vapor pressure of the second metal-iodide (M2)I_y be much larger than that of the first. It is also necessary that the hetero-complex form in the desired temperature range. Complexes can also form in the condensed phases.

Many pairs of metal-halide salts that exhibit evaporation enhancement through complexation are known and have been investigated.¹ However, almost none of this work has involved metal-iodide pairs and temperature ranges of relevance to metal-halide lamps. Nevertheless, the effects described above have long been used to improve the performance of metal-halide lamps.²

We recently studied the evaporation characteristics of DyI₃ when mixed with InI and of TmI₃ when mixed with TlI.³ The evaporation of both of these lanthanides was seen to be strongly enhanced over the mixtures, and this was attributed to the formation of the vapor-phase hetero-complexes DyInI₄ in the first case, and TmTlI₄ in the latter. Liquid-phase complexes were also seen to be important.

Here, we continue our investigations of lanthanide iodides and possible complexing pairs by examining the effect of three Group 13 metal-halides on the evaporation characteristics of CeI₃. GaI₃, InI, and TlI, in pure form, each possesses a vapor pressure considerably higher than pure CeI₃ and is thus a potential candidate for enhancing the content of Ce in the vapor phase through complex formation. We observed CeI₃, CeI₃/GaI₃, CeI₃/InI, and CeI₃/TlI for temperatures up to 1400 K using x-ray induced fluorescence to measure the total densities Ce and I in the first two systems,

^{a)}Electronic mail: jjcurry@nist.gov

^{b)}Present Address: Lucidity Lights, 218 W. Cummings Park, Woburn, MA 01801, USA.

^{c)}Also at Henins Enterprises, 0628 Seneca Spring Way, Gaithersburg, MD 20886, USA.

Ce, I, and In in the third system, and Ce, I, and Tl in the fourth system. An improvement in our calibration method has reduced measurement uncertainties relative to those in our previous work.

The data presented will help guide the development of new HID lamp designs by improving the accuracy of lamp modeling. The data will also be of interest to those compiling thermodynamic parameters, especially since it covers systems and temperatures where little or no data currently exist.

II. DESCRIPTION OF METHODS

The use of x-ray induced fluorescence (XRIF) to measure vapor pressures is discussed in depth by two previous publications.^{3,4} Many details given there will not be repeated here.

XRIF, as we use it, is largely insensitive to the chemical state of an atom. It therefore provides a measure of the total number density of each element (designated by the subscript Z) summed over all atomic and molecular species M_i containing that element

$$n_Z = \sum_i c_{Zi} M_i, \quad (2)$$

where c_{Zi} is the corresponding stoichiometric coefficient. The measurement of total density as defined by Eq. (2) is of particular relevance to the measurement of vapor-phase enhancement because no assumptions need be made regarding the various molecular species in which a particular element may be distributed. For example, XRIF is able to tell

us directly how much extra Ce can be put into the vapor phase, at a given temperature, by adding InI to CeI₃.

A vapor pressure corresponding to the total number density of each element can be defined as

$$p_Z = n_Z kT = kT \sum_i c_{Zi} M_i, \quad (3)$$

using Boltzmann's constant k and the measured vapor temperature T . This definition should not be confused with an actual total or partial pressure, since in general, $c_{Zi} > 1$. An advantage of this definition is that it corresponds directly to the measured total density n_Z . Figure 1 is a schematic showing the measurement of vapors by XRIF. A highly collimated, mono-energetic x-ray beam, obtained from the Sector 1 Insertion Device beamline⁵ at the Advanced Photon Source, was used to induce fluorescence in the vapor to be studied. The vapor was produced by heating salts contained in a sealed ceramic or fused quartz cell (Figure 2). The resulting x-ray fluorescence was observed with an energy-resolving germanium detector, producing spectra like those in Figure 3. A pair of x-ray apertures was used to limit the detector field-of-view to a narrow cone that intersected the main x-ray beam inside the center of the vapor cell. One of these apertures was immediately in front of the detector and is shown in Figure 1. The other aperture can only be seen in the close up of the vapor cell enclosed in its tantalum jacket, in Figure 4.

Table I lists the cells used in the measurements described here. Most of the cells are made from polycrystalline alumina (PCA) because PCA is highly resistant to corrosion from

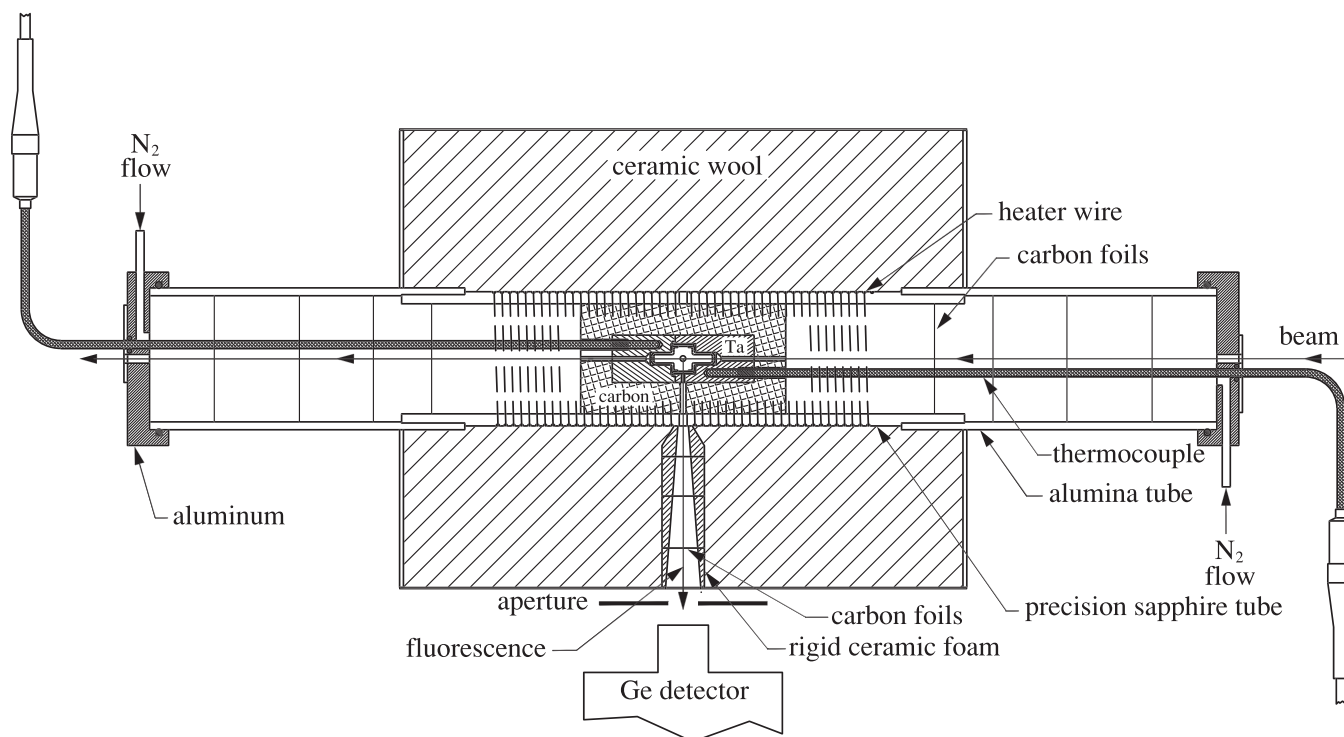


FIG. 1. Schematic of experiment for measuring vapor-phase densities with x-ray induced fluorescence. The vapor cell was held inside an oven in a tantalum jacket. A graphite tube filled the space between the outer diameter of the tantalum and the inner diameter of a sapphire tube. Heat was provided by a resistive wire wound around the sapphire tube and driven by a direct current. Carbon foils reduced heat loss by convection along the tube and through a fluorescence exit hole. A nitrogen purge prevented oxidation. Thermocouples measured the temperature at two locations in the tantalum.

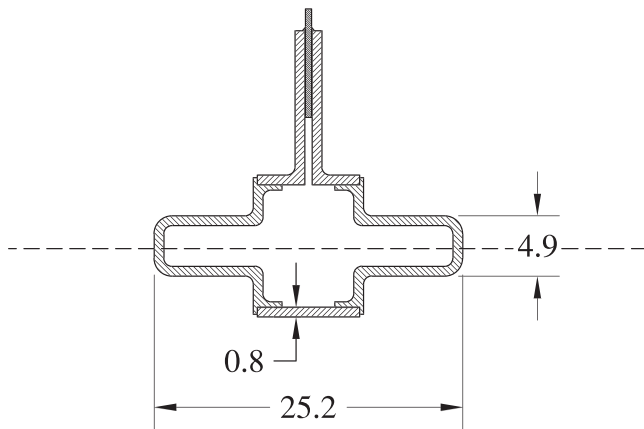


FIG. 2. Cross section of a PCA vapor cell, with dimensions in millimeters. The cell is cylindrically symmetric about the axis shown except for a filling capillary at the top. In Figures 1 and 4, the cell is rotated about the beam axis so that the filling stem points out of the page.

complex mixtures of metal-halide salts at elevated temperatures.¹⁷ The cells were prepared by extended baking under vacuum, injection with a dose of metal-halide salts through the open capillary, back-filled with several kPa of Xe, then permanently sealed by inserting a PCA rod and low-temperature frit into the capillary and locally heating to a temperature sufficient to achieve a permanent seal. Two cells were made from fused quartz in order to test the suitability of quartz for future measurements. Quartz is less resistant to corrosion, but quartz cells are easier to manufacture than PCA cells.

Number densities for each element were obtained by integrating the number of detector counts in the corresponding peaks of the fluorescence spectra (Figure 3). In previous work, we showed how a measurement n_Z can be put on an absolute density scale by comparison to a Xe density standard n_{Xe} ¹⁸ by

$$n_Z = \frac{C_Z^{K\eta}}{C_{Xe}^{K\alpha}} \frac{\Phi_i(Xe)}{\Phi_i(Z)} \frac{\sigma_{Xe}^K(E_i)}{\sigma_Z^K(E_i)} \frac{Y_{Xe}^K}{Y_Z^K} \frac{B_{Xe}^{K\alpha}}{B_Z^{K\eta}} \frac{\tau(E_{Xe}^{K\alpha})}{\tau(E_Z^{K\eta})} \frac{Q_d(E_{Xe}^{K\alpha})}{Q_d(E_Z^{K\eta})} n_{Xe}, \quad (4)$$

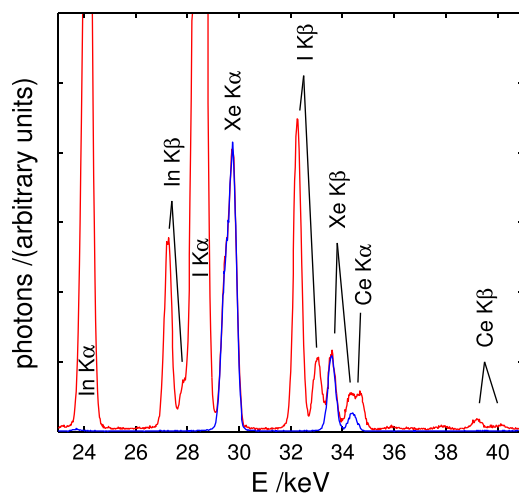


FIG. 3. Two fluorescence spectra from a cell containing CeI_3/InI with Xe. The blue spectrum was acquired while the lamp was at room temperature, the red spectrum while the cell temperature was near 1320 K. The spectra have been normalized so that Xe intensity is the same in both.

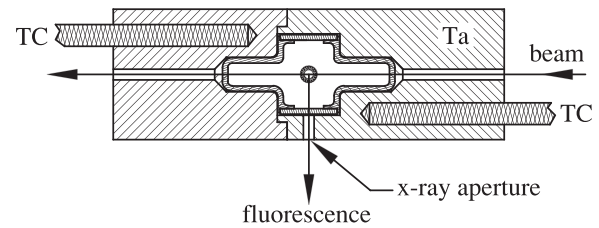


FIG. 4. Vapor cell jacketed by tantalum. The latter absorbed scattered x rays and provided a more uniform temperature distribution over the cell. Type-N thermocouples (TC) were inserted into two holes in the tantalum, one in the upper left and one in the lower right. A small hole, shown at the bottom of the figure, allowed x-ray fluorescence to escape toward the Ge detector.

where $C_Z^{K\eta}$ is the number of counts in the $K\eta$ fluorescence line of element Z , Φ_i is the incident x-ray flux, σ^K is the K-shell photo-electric absorption cross section, E_i is the incident beam energy, Y^K is the K-shell fluorescence yield, $B^{K\eta}$ is the relative strength of the $K\eta$ line relative to the other K-shell lines, $\tau(E)$ is the transmission through the cell wall at energy E , and Q_d is the quantum efficiency of the detector. At that time, we used an external standard consisting of a nominally identical cell filled only with Xe, which we periodically substituted for the vapor cells containing salts. A weakness of that approach was that the vapor cell and tantalum jacket, when held in the oven, did not have a well-defined position relative to the detector. Expansion and shifting of the oven as it progressed through its temperature excursions and back to room temperature were also a problem. The sensitivity of the detected fluorescence to such movement undoubtedly originates with the relatively small fluorescence collection hole in the tantalum.

Here, we substantially improve our absolute calibration by using an internal standard created by putting Xe into the vapor cells with the metal-halide salts of interest. In this case, movement of a cell and tantalum jacket does not alter the calibration because the Xe fluorescence and metal-halide vapor fluorescence are affected identically. The same applies to changes in the incident beam flux, so it is no longer necessary to monitor that quantity, and absolute elemental densities can be determined from the slightly simpler expression

$$n_Z = \frac{C_Z^{K\eta}}{C_{Xe}^{K\alpha}} \frac{\sigma_{Xe}^K(E_i)}{\sigma_Z^K(E_i)} \frac{Y_{Xe}^K}{Y_Z^K} \frac{B_{Xe}^{K\alpha}}{B_Z^{K\eta}} \frac{\tau(E_{Xe}^{K\alpha})}{\tau(E_Z^{K\eta})} \frac{Q_d(E_{Xe}^{K\alpha})}{Q_d(E_Z^{K\eta})} n_{Xe}. \quad (5)$$

Figure 3 shows fluorescence spectra from cell C11, which was nominally dosed with 6.8 mg of CeI_3 , 3.2 mg of InI , and 13 kPa of Xe. The spectrum in blue was obtained while the cell was at room temperature, and it shows only the 3 peaks from the Xe internal standard. The vapor density of other elements at room temperature is too low to be measured. The spectrum in red was acquired when the cell temperature was approximately 1320 K. At this high temperature, all of the elements are present in the vapor phase in one form or another, with In and I being more abundant than Xe. Ce is present as well, but in much lower quantity. The magnitude of the second spectrum has been normalized so that the Xe peaks match those in the first spectrum.

TABLE I. Details of observed vapor cells and select results. The cell volume is $7.3(\pm 0.7) \times 10^{-7} \text{ m}^3$. All uncertainties are standard uncertainties.

Cell No. ^a	Salt mixture	Target quantities/mg ^b	Simulated quantities/mg	Simulated mole fraction ^c	Target Xe pressure/kPa ^d	Measured Xe pressure/kPa ^d	$\log_{10}(p_{Ce}/\text{Pa})^e$
C1	none	67	36.8 ± 0.9	
Q1	none	67	39.6 ± 0.8	
Q4	CeI ₃	9.99	13	12.7 ± 0.8	$11.74(\pm 0.04) - 11,210(\pm 60) (T/K)^{-1}$
C4	CeI ₃ /GaI ₃	9.21/0.807	9.2/0.72	0.083	13	8.1 ± 0.5	$11.72(\pm 0.06) - 11,200(\pm 80) (T/K)^{-1}$
C8	CeI ₃ /GaI ₃	5.38/4.64	5.4/2.0	0.30	13	2.50 ± 0.16	$10.7(\pm 0.2) - 9,900(\pm 300) (T/K)^{-1}$
C9	CeI ₃ /InI	9.58/0.465	6.3/0.50	0.15	13	6.9 ± 0.4	$11.05(\pm 0.04) - 10,210(\pm 60) (T/K)^{-1}$
C11	CeI ₃ /InI	6.84/3.17	5.9/2.9	0.51	13	7.3 ± 0.5	$9.65(\pm 0.08) - 8,096(\pm 100) (T/K)^{-1}$
C14	CeI ₃ /TlI	9.40/0.594	5.5/0.66	0.16	13	9.8 ± 0.6	$10.38(\pm 0.09) - 9,320(\pm 120) (T/K)^{-1}$
C15	CeI ₃ /TlI	6.11/3.87	9.5/6.1 ^f	0.50	13	11.0 ± 1	$10.11(\pm 0.06) - 8,650(\pm 80) (T/K)^{-1}$
C17	CeI ₃	10.0	13	8.0 ± 0.6	$11.59(\pm 0.03) - 11,010(\pm 50) (T/K)^{-1}$

^a“C” designates a ceramic cell, ‘Q’ designates a fused quartz cell.

^bNominal values.

^cOf the minority component.

^dAt standard temperature.

^eLeast-squares fit to the data.

^fWe also included 1.9 μg of H₂O.

The use of an internal standard eliminates sources of error that originate from long-term drifts in experimental conditions, but the systematic uncertainty in the measured elemental densities can be no better than the determination of the Xe density in each cell. Our previous experience demonstrated that the Xe density must be determined by an independent measurement after the cell is filled because the sealing process can greatly affect the actual fill pressure. X-ray absorption can provide an accurate measurement if the absorber density is large enough. Thus, we made one PCA cell (C1 in Table I) and one fused quartz cell (Q1), both containing Xe only, with a nominal pressure of 70 kPa, enough to absorb about 5% of a 50 keV beam. We then measured the actual density in these cells using the apparatus in Figure 5 and monitoring the transmitted beam flux as we alternately condensed and evaporated the Xe. Xe was condensed in the lower section of the cell by allowing that end to rest in a liquid nitrogen reservoir. If the reservoir was not replenished, the liquid nitrogen boiled away in a few minutes allowing the Xe to evaporate and fill the cell. Figure 6 shows the ratio of signal from the upstream ionization chamber to the signal from the downstream p-i-n diode detector during this sequence. The initial constant level is proportional to the apparatus transmission without Xe. The final (nearly) constant level is proportional to the transmission with Xe. The ratio of the two is the transmission through the Xe only

$$T_{Xe} = \exp(-n_{Xe}\sigma_{Xe}l). \quad (6)$$

The Xe cross section at 50 keV $\sigma_{Xe} = 2.72(\pm 0.02) \times 10^{-25} \text{ m}^2$ includes the total photoelectric cross section as well as partial contributions from the coherent and incoherent cross sections.⁶ The absorption path length l is the distance across the diameter of the body of the cell. By this method, we determined the density of Xe in C1 and Q1 with a standard uncertainty of $\pm 3\%$. The actual pressures (at standard temperature) were less than half the 70 kPa target pressures for these cells.

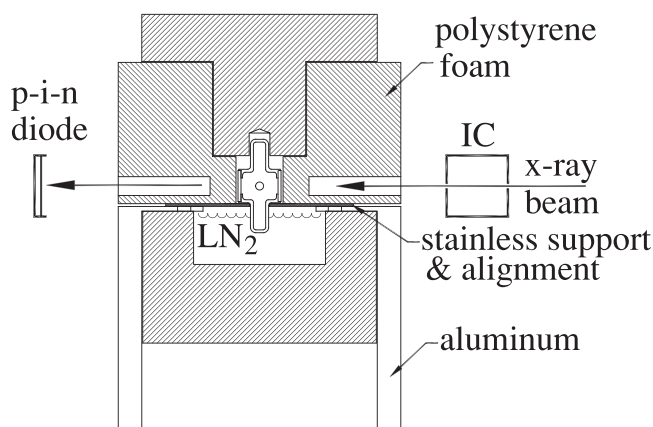


FIG. 5. The apparatus used to determine the absolute Xe densities in C1 and Q1 using x-ray absorption. LN₂ designates the liquid nitrogen reservoir, while IC designates the ionization chamber used for measuring the incident flux. Liquid nitrogen was used to condense Xe in the bottom of the cell. When the liquid nitrogen boiled away, the Xe quickly evaporated, changing the transmitted intensity by a couple of percent.

The Xe densities in the vapor cells were obtained by comparison of Xe fluorescence intensities from cells C1 and Q1. The apparatus in Figure 7 overcame much of the difficulty with fluorescence comparisons in our previous work by positioning the cells and tantalum jacket reproducibly with respect to the detector. A v-block and a removable alignment pin tightly constrained the position and angle of the cell and jacket. Fluorescence measurements of C1 on 7 separate occasions were reproducible to better than 5% mean standard deviation, about half the mean standard deviation seen when the cells were held by the oven. This reproducibility is included in the uncertainties for the Xe pressures measured by fluorescence and given in Table I.

The measurements presented here differ from previous measurements in that the power to the oven was controlled by a computer in such a way as to keep the rate of temperature change nearly constant in time at a level of less than

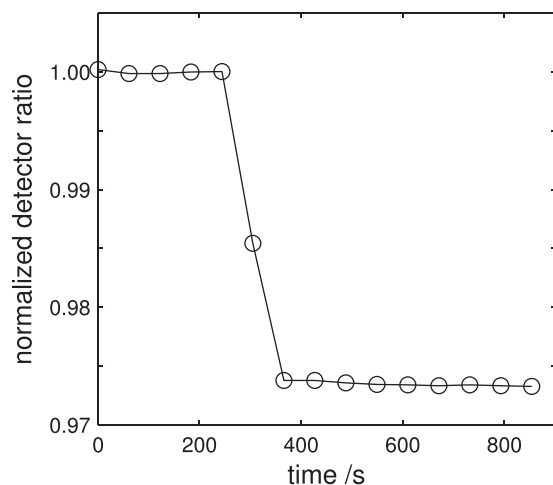


FIG. 6. Typical time dependence of the normalized detector ratio used to determine the Xe density in cell C1. The Xe is initially condensed out of the x-ray beam, but begins to evaporate around $t = 250$ s. It is completely evaporated by $t = 370$ s.

0.032 K/s. Nearly all measurements were made with the time rate of change in the temperature of less than 0.02 K/s. This small rate of change is significantly less than the rates we determined in our previous work to be sufficiently small for our measurements to reflect equilibrium values. The integration time for each data point was 30 s.

Temperature values were determined by a pair of type-N thermocouples as shown in Figures 1 and 4. The thermocouples were connected to a pair of identical nano-volt meters through an identical pair of zero-point junctions.

We have interpreted some of our measurements with numerical modeling of the thermochemical equilibrium within each test cell, including investigating the importance of various molecular species and the compatibility of existing thermochemical data with our results. Our model, based on the algorithm of Cruise,⁷ utilizes the free energies of formation of all molecular species to compute a self-consistent set of the numbers of each molecule in a closed system. Assumptions are pure solids, ideal liquids, and ideal vapors. For the highest temperatures investigated, the total pressures in our calculations are comparable to, but do not significantly exceed, 10^5 Pa where non-ideal behavior begins to become apparent. Input parameters are temperature, cell volume, salt dose in the cell, and free energies of formation ($\Delta_f G^\circ(T)$) of all molecular phases to be considered.

A limitation of such modeling is that we do not always know what species exist in a system. Our measurements do not provide us with a molecular inventory and little or no previous work on these systems is available. Many species are obvious, but it is sometimes clear that unknown species are also present. Where data are available, we have used the JANAF Tables,⁸ Barin's compilation,⁹ the compilation of vapor pressure data by Hansen *et al.*,¹⁰ and Ohnesorge's recent investigation of lanthanide-iodide vapors.¹¹ Where no data are available, we deduce reasonable values by requiring the model to reproduce the measurements as closely as possible.

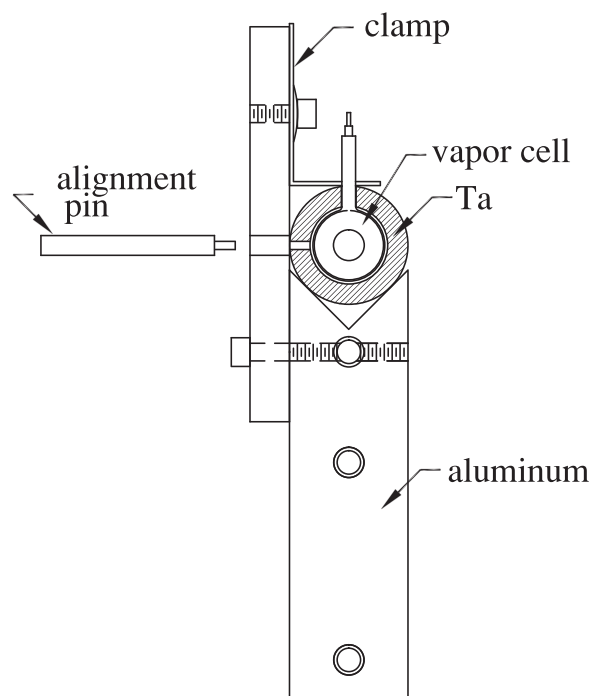


FIG. 7. The apparatus used to compare Xe fluorescence intensities. The v-block and removable alignment pin enabled reproducible positioning of the fluorescence cells. The incident beam is going into the page and fluorescence is observed to the left through the same hole used by the alignment pin. The tantalum jacket is the same as that shown in Figure 4.

III. RESULTS AND DISCUSSION

A. CeI_3

Vapor pressures corresponding to the total densities of Ce in cells Q4 and C17, both dosed only with CeI_3 and Xe, are shown in Figure 8. Also shown is the analytic expression given by Hansen *et al.*¹⁰ for the vapor pressure of CeI_3 above its melting point, based on optical absorption measurements made by Liu and Zollweg.¹² The highest temperature for which the latter obtained a measurement was about 1135 K. The melting point of CeI_3 given by Hansen *et al.*¹⁰ is 1033 K.

The measurements from Q4 and C17 are similar (Figure 8). Linear fits to $\log_{10}(n_{Ce}kT)$ in the variable $1/T$ for both sets of data show a maximum pressure difference of 6%. A fit to the combined data from both cells gives

$$\log_{10} p_{Ce}/\text{Pa} = 11.65(\pm 0.03) - 11,090(\pm 40) \times (T/\text{K})^{-1}. \quad (7)$$

Measurements of I in these cells are shown in Figure 9 and indicate possible contamination and/or interactions with cell material. Data from cell C17 is most interesting, with two separate dips in the vapor pressure corresponding to the total density of I. In previous work,³ we described how a dip in the vapor pressure can occur when a multi-component liquid melt forms near the normal melting temperature of the primary component. Here, the deepest minimum in the I content occurs near the melting temperature of pure CeI_3 , shown by the vertical dashed line in the figure.

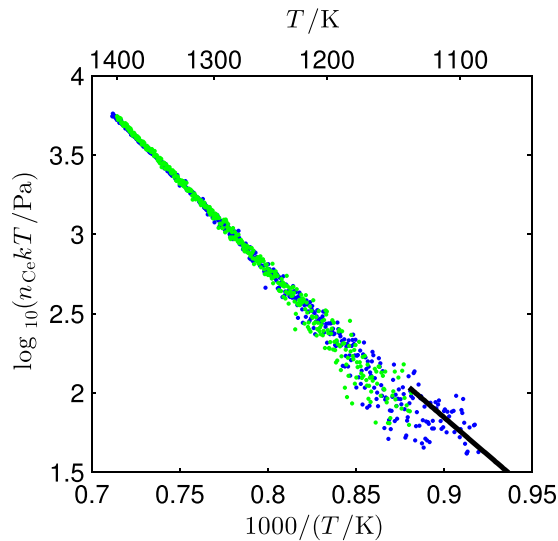


FIG. 8. Measured vapor pressures corresponding to total densities of Ce in cells Q4 (green) and C17 (blue) dosed only with CeI₃ and Xe. The black line is the analytic expression of Hansen¹⁰ derived from the measurements of Liu and Zollweg.¹²

A smaller minimum in the I content occurs near $T \approx 875$ K. We cannot suggest a likely component that normally melts at this temperature. If another element is present in the cell, it is lighter than Kr or heavier than Tm. Otherwise, it would be observed by XRIF.¹⁹

The I content in Q4 is also elevated at lower temperatures, but does not give indications of any dips, at least in the temperature ranges where data were acquired. We previously showed,³ with numerical modeling, that a small amount of water contamination in the cell can produce excess levels of I at low temperatures, due to the formation of the volatile molecule HI.

The other interesting behavior associated with I is the I:Ce ratio. It differs between the two cells and in neither case is it the expected stoichiometric value of 3:1. (We observed similar anomalous behavior in DyI₃, DyI₃/InI, TmI₃, and TmI₃/TII systems.³) In C17, the ratio varies from 14:1 at

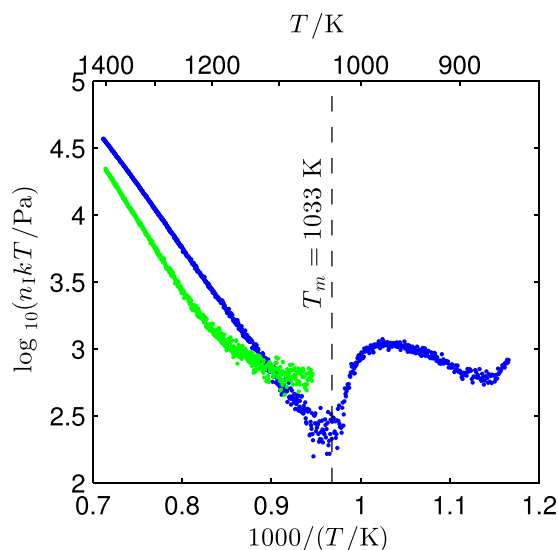
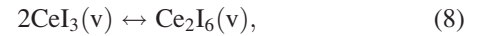


FIG. 9. Measured vapor pressures corresponding to total densities of I in cells Q4 (green) and C17 (blue) dosed only with CeI₃ and Xe.

$T \approx 1100$ K to 6:1 at $T \approx 1400$ K. In Q4, the ratio varies from 5:1 at $T \approx 1250$ K to 4:1 at $T \approx 1400$ K.

The close agreement for Ce in the two cells, despite markedly different behavior for I, and the agreement with Hansen's expression suggest that the Ce measurements from both cells reflect the true evaporation behavior of pure CeI₃.

Our measurements of the vapor pressure corresponding to the total density of Ce include possible contributions from the vapor-phase dimer Ce₂I₆. It is not clear whether the measurements of Liu and Zollweg include such contributions. Ohnesorge¹¹ derived an expression for the temperature dependence of the equilibrium constant for dimer formation



from his measurements at temperatures below 1017 K

$$\log_{10}(K) = \log_{10} \frac{p[\text{Ce}_2\text{I}_6]/10^5 \text{Pa}}{(p[\text{CeI}_3]/10^5 \text{Pa})^2} = -5.700 + \frac{8829}{(T/\text{K})}. \quad (9)$$

Figure 10 gives the partial pressures of the monomer and dimer that may be derived from the combined measurements in Q4 and C17 using Ohnesorge's expression and

$$p_{\text{Ce}} = p[\text{CeI}_3] + 2p[\text{Ce}_2\text{I}_6], \quad (10)$$

for the measured vapor pressure corresponding to the total density of Ce. As seen in Figure 10, the dimer pressure is always far smaller than the monomer pressure, but becomes more prominent with increasing temperature, contributing 7% to the total Ce content at $T \approx 1150$ K and 12% at $T \approx 1400$ K.

A fit to the monomer partial pressure produces the expression

$$\log_{10}(p[\text{CeI}_3]/\text{Pa}) = 11.24(\pm 0.03) - 10,690(\pm 40)/(T/\text{K}). \quad (11)$$

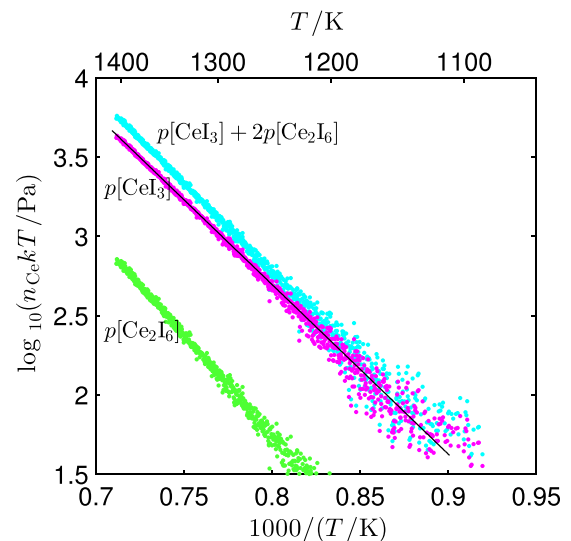


FIG. 10. Measured vapor pressure corresponding to the total vapor density of Ce in cells Q4 and C17 nominally containing only CeI₃ and Xe. Also shown are the partial pressures of the CeI₃ monomer and the Ce₂I₆ dimer, with a linear fit to the monomer partial pressure (black line).

TABLE II. Free energies of formation used in thermochemical equilibrium calculations for systems containing CeI₃ over the temperature range 900 K to 1400 K.

Molecule	$\Delta_f G^\circ(T)/(J/mol)$	Source
CeI ₃ (s)	$-752\,400 + 227.3T + 6.134 \times 10^{-3} T^2$	Barin ⁹ and Hansen <i>et al.</i> ^{10a}
CeO ₂ (s)	$-1\,087\,000 + 206.3T$	Barin ⁹
CeI ₃ (l)	$-673\,100 + 150.6T + 6.134 \times 10^{-3} T^2$	present measurements ^b
CeInI ₄ (l)	$-841\,000 + 215T$	present measurements ^b
CeTlI ₄ (l)	$-844\,000 + 200T$	present measurements ^b
CeI ₃ (v)	$-468\,400 + 30.94T + 6.134 \times 10^{-3} T^2$	Barin ⁹
Ce ₂ I ₆ (v)	$-1\,106\,000 + 171.0T + 1.227 \times 10^{-2} T^2$	Ohnesorge ¹¹ and Barin ⁹
CeInI ₄ (v)	$-659\,500 + 95T$	present measurements ^b
CeTlI ₄ (v)	$-769\,000 + 180T$	present measurements ^b
CeTl ₂ I ₅ (v)	$-759\,000 + 70T$	present measurements ^b
InI(l)	$-126\,100 + 32.15T$	Barin ⁹
InI(v)	$-35\,300 - 57.90T$	Barin ⁹
In ₂ I ₂ (v)	$-155\,800 + 13.70T$	Ohnesorge ¹¹ and Barin ⁹
TlI(l)	$-139\,100 + 25.63T - 5.988 \times 10^{-3} T^2$	Barin ⁹ and Hansen <i>et al.</i> ¹⁰
TlI(v)	$-29\,090 - 74.74T + 5.988 \times 10^{-3} T^2$	Barin ⁹
Tl ₂ I ₂ (v)	$-150\,300 - 27.30T + 0.01198 T^2$	Ohnesorge ¹¹ and Barin ⁹
I(v)	$78\,190 - 53.82T$	JANAF Tables ⁸
I ₂ (l)	$-46\,920 + 116.4T - 0.03018 T^2$	JANAF Tables ⁸
I ₂ (v) ^c	0	JANAF Tables ⁸
H ₂ O(l)	$-283\,300 + 155.2T$	JANAF Tables ⁸
H ₂ O(v)	$-241\,200 + 43.41T + 4.959 \times 10^{-3} T^2$	JANAF Tables ⁸
H(v)	$222\,100 - 56.87T$	JANAF Tables ⁸
H ₂ (v) ^d	0	JANAF Tables ⁸
HI(v)	$-6517 - 7.211T$	JANAF Tables ⁸
O(v)	$252\,300 - 64.80T$	JANAF Tables ⁸

^aAdjusted by +300 J/mol in order to make the melting temperature approximately 1030 K.

^bObtained by optimizing agreement between calculations and present measurements.

^cI₂(v) is the reference state for $T > 458$ K.

^dH₂(v) is the reference state for $T > 20$ K.

The numbers in parentheses reflect the uncertainties arising from random sources only. (Systematic uncertainties in our measurements will be discussed in Sec. IV.) This expression, combined with the free energy of formation for the monomer,⁹ allows us to determine the free energy of formation for liquid CeI₃. A free energy of formation for the dimer may be obtained by combining the free energy of formation for the monomer with Ohnesorge's equilibrium constant Equation (9). All of these expressions are given in Table II.

B. CeI₃/GaI₃

Measurements of the vapor pressures corresponding to the total densities of Ce and I in cells containing mixtures of CeI₃ and GaI₃ (cells C4 and C8) are shown in Figure 11, along with results from our numerical model. Observations of Ga are not shown because the x-ray fluorescence emitted by Ga occurs at energies (<10.3 keV) too low to be transmitted through the cell wall. Data for cell C8, containing the higher concentration of GaI₃, were acquired over the limited temperature range of approximately 1255 K to 1330 K. Time constraints prevented acquisition at higher temperatures, while high count rates from I introduced by GaI₃ reduced the signal-to-noise ratio of the Ce measurements at lower temperatures. Despite the limited temperature range, we are still able to observe the trend for Ce in cell C8, which agrees well

with observations in Q4, C4, and C17. GaI₃, at the concentrations examined, has no measurable effect on the evaporation of CeI₃ above the melting temperature of CeI₃.

We are able to closely reproduce both the Ce and I observations in both cells using our numerical model

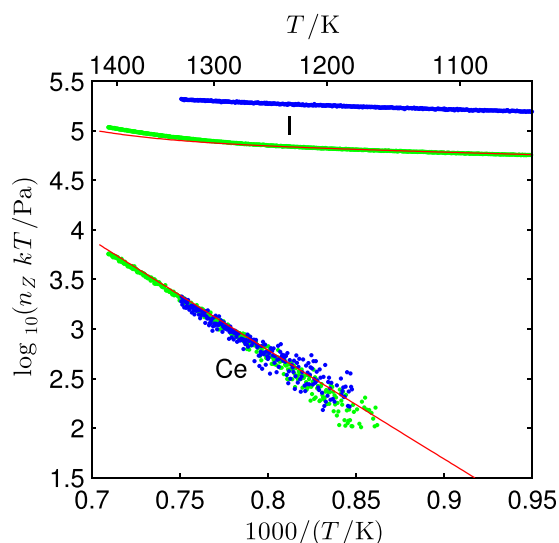


FIG. 11. Measured vapor pressures corresponding to total densities of Ce and I in cells C4 (green) and C8 (blue), both dosed with CeI₃ and GaI₃. Numerical predictions are shown in red for C4.

including only the molecules $\text{CeI}_3(\text{s,l,v})$ and $\text{GaI}_3(\text{l,v})$. The modeling results for Ce reflect our measurements in cells Q4 and C17 because of our choice for the free energy of formation for $\text{CeI}_3(\text{l})$. In both cells C4 and C8, the quantity of I in the vapor saturates at temperatures below 500 K, consistent with the complete evaporation of the GaI_3 dose. If the I is present only in the form of GaI_3 , this gives a clear indication of the GaI_3 dose in each cell. We needed 0.72 mg of GaI_3 to numerically reproduce the iodine observations in C4 and 2.0 mg of GaI_3 to reproduce the observations in C8. The latter value is far below the target value given in Table I. The free energies of formation for the GaI_3 phases do not play a role in our calculations since the GaI_3 is completely evaporated in the range of temperatures we observed and we do not include any interactions (complexes) with CeI_3 . Therefore, these data are not included in Table II.

C. CeI_3/InI

The vapor pressures corresponding to the total densities of Ce in cells C9 and C11, each containing a mixture of CeI_3 and InI, are shown in Figure 12. Also shown, for reference, is the fit to the Ce measurements from cells Q4 and C17, combined, each containing only CeI_3 . Enhancement of the Ce content is seen in both cases, but is larger in C11, which contains the larger molar ratio of InI. The largest enhancement observed is more than a factor of 5. In both cases, the enhancement is stronger at lower temperatures, decreasing with increasing temperature. Fits to the data are shown in the figure and are given in Table I.

Looking at the behavior of I and In in these cells is also useful. Figure 13 shows observations for Ce, In, and I in cell C9, as well as the vapor pressure for pure InI as given by Hansen *et al.*¹⁰ and predictions from our numerical model. The dramatically lower vapor pressure observed for In as compared to the pure InI vapor pressure is an indicator of a liquid phase complex that dilutes the liquid melt. The minima

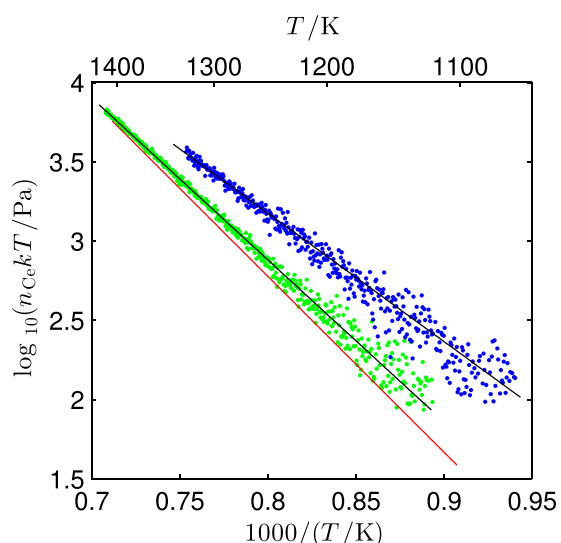


FIG. 12. Measured vapor pressures corresponding to the total densities of Ce in cells C9 (green) and C11 (blue) containing different mixtures of CeI_3 and InI. The data are compared to a fit to the equivalent combined measurements in Q4 and C17 containing only CeI_3 (red). Fits to the data from C9 and C11 are also shown for clarity (black).

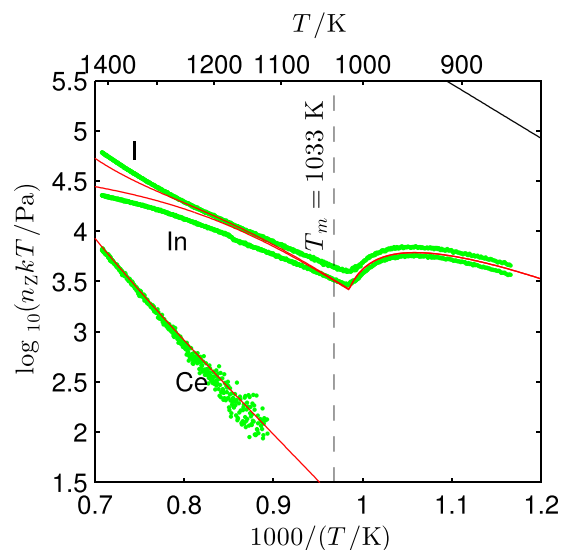


FIG. 13. Measured vapor pressures corresponding to the total densities of Ce, In, and I in cell C9 nominally containing 9.58 mg of CeI_3 and 0.465 mg of InI. The vapor pressure for pure InI is shown by the black curve¹⁰ in the upper right corner. Predictions from our numerical model assuming 6.3 mg of CeI_3 and 0.50 mg of InI are shown by the red curves.

in the pressures for In and I near the melting temperature of CeI_3 indicate the continued presence of a liquid condensate up to and through the melting temperature of CeI_3 . The dilution factor from melting CeI_3 is much stronger than from the liquid-phase complex. The presence of a liquid condensate leading up to the melting temperature also induces CeI_3 to melt at lower temperatures, so that dilution happens gradually.

The complete observations in cell C11 along with numerical predictions are shown in Figure 14. Here, the larger molar ratio of InI substantially reduces the dilution of the condensate by CeI_3 , which melts completely at temperatures below 900 K. No minimum in the In and I content is observed.

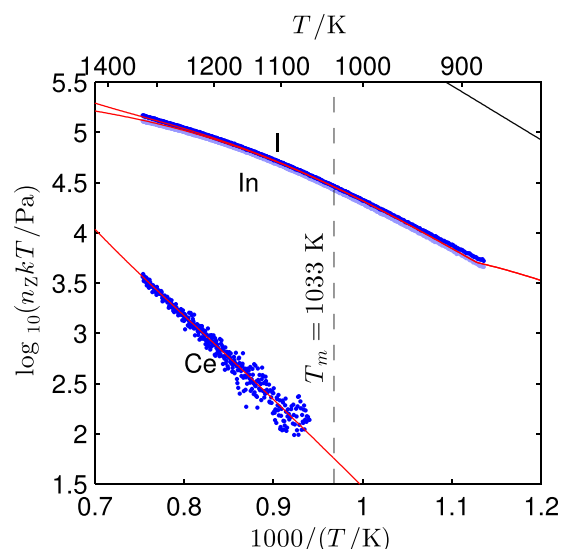


FIG. 14. Measured vapor pressures corresponding to the total densities of Ce, In, and I in cell C11 nominally containing 6.84 mg of CeI_3 and 3.17 mg of InI. The vapor pressure for pure InI¹⁰ is shown by the black curve in the upper right corner. Predictions from our numerical model assuming 5.9 mg of CeI_3 and 2.9 mg of InI are shown by the red curves.

We have been able to largely reproduce these observations with our numerical model by hypothesizing the existence of the complex CeInI_4 in both the liquid and vapor phases. Free energies of formation for each phase were determined by matching our calculations to our observations in both C9 and C11 as closely as possible. In previous work,³ we showed how the model predictions changed when complexes were not included in the DyI_3/InI system, which exhibits similar behavior. Our calculations included $\text{CeI}_3(\text{s,l,v})$, $\text{Ce}_2\text{I}_6(\text{v})$, $\text{InI}(\text{l,v})$ and $\text{In}_2\text{I}_2(\text{v})$ in addition to the hetero-complexes $\text{CeInI}_4(\text{l})$ and $\text{CeInI}_4(\text{v})$. All of these free energies of formation can be found in Table II.

Barin⁹ gives values for $\text{CeI}_3(\text{s})$, but when combined with our values for the liquid, they give a melting temperature close to 1040 K, higher than the observed minima in our measured vapor pressures. In order to obtain better agreement with our observations, we add 300 J/mol to Barin's values for $\text{CeI}_3(\text{s})$. In fact, Barin's values for both the liquid and solid phases give a melting temperature closer to 1100 K! It is also interesting to note that the expressions by Hansen *et al.*¹⁰ for CeI_3 vapor pressures over the solid and liquid phases also indicate a melting temperature near 1100 K. The melting point tabulated by Hansen *et al.* is 1033 K.

The modelling predictions in Figures 13 and 14 required adjustment of the quantities of both CeI_3 and InI in each cell. The modified values are given in Table I.

D. CeI_3/TlI

The vapor pressures corresponding to the total densities of Ce in the CeI_3/TlI system are shown in Figure 15 for two different mole fractions. The nominal TlI mole fractions are 0.09 (cell C14) and 0.5 (cell C15). The red line in the figure is the fit to the combined Ce data sets from cells Q4 and C17, each containing only CeI_3 . The black lines are fits to the data from cells C14 and C15. These fits are given in

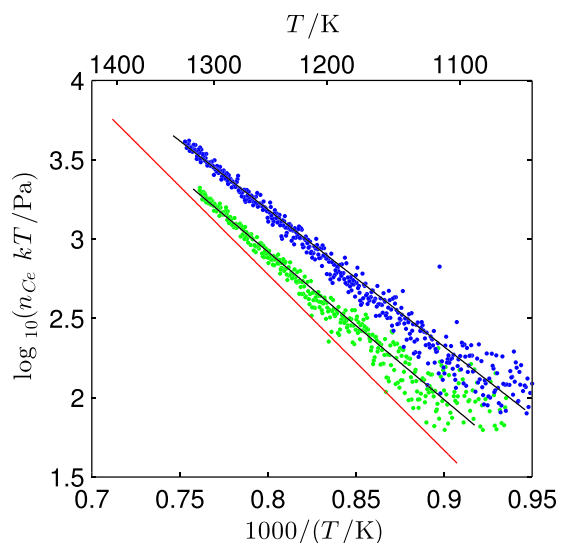


FIG. 15. Measured vapor pressures corresponding to the total densities of Ce in cells C14 (green) and C15 (blue) containing different mixtures of CeI_3 and TlI. The data are compared to a fit to the equivalent combined measurements in Q4 and C17 containing only CeI_3 (red). Fits to the data from C14 and C15 are also shown for clarity (black).

Table I. Both molar ratios yield enhancement of the Ce content, with the higher molar ratio of TlI giving significantly more enhancement. The enhancement in C15 is about a factor of 5 at $T = 1100$ K, diminishing with increasing temperature, as was the case with CeI_3/InI .

Simulation of the principal features of the CeI_3/TlI system observed in cells C14 (Figure 16) and C15 (Figure 17) required inclusion of two liquid-phase complexes and one vapor-phase complex. The suppressed Tl and I content relative to the equilibrium vapor pressure for pure TlI (black curve in both figures) indicates the action of a liquid complex (we postulated $\text{CeTlI}_4(\text{l})$), while the enhanced Ce content indicates a vapor phase complex (we postulated

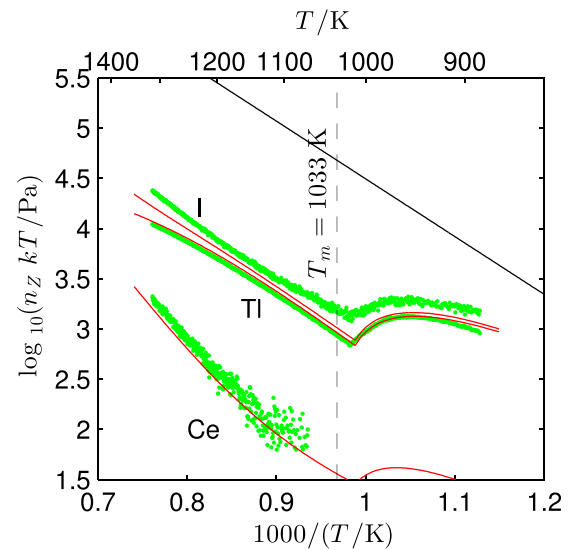


FIG. 16. Measured vapor pressures corresponding to the total densities of Ce, Tl, and I in cell C14 nominally containing 9.4 mg of CeI_3 and 0.59 mg of TlI. The vapor pressure for pure TlI¹⁰ is shown by the black curve. Predictions from our numerical model assuming 5.5 mg of CeI_3 and 0.66 mg of TlI are shown by the red curves.

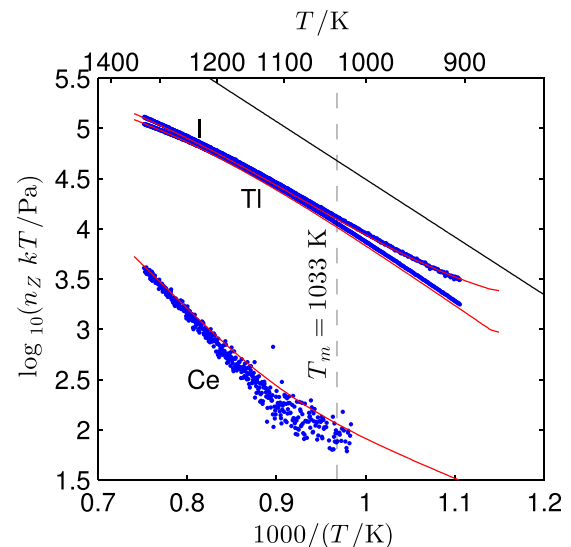


FIG. 17. Measured vapor pressures corresponding to the total densities of Ce, Tl, and I in cell C15 nominally containing 6.1 mg of CeI_3 and 3.9 mg of TlI. The vapor pressure for pure TlI¹⁰ is shown by the black curve. Predictions from our numerical model assuming 9.5 mg of CeI_3 , 6.1 mg of TlI, and 1.9 μg of H_2O are shown by the red curves.

CeTlI₄(v)). However, we were not able to reproduce the distinct change in slope of the Ce curve, most clearly observed in cell C15, using only 2 complexes. Agreement between our observations and numerical predictions improved substantially after we introduced a second liquid complex, CeTl₂I₅(l). Additionally, we added a small amount of H₂O to our simulations of C15 in order to reproduce the elevated levels of I, relative to Tl at the lower temperatures. The masses of CeI₃, TlI, and H₂O used in our simulations are given in Table I, while the free energies of formation for the allowed molecular species are given in Table II.

IV. MEASUREMENT ERRORS AND UNCERTAINTIES

All uncertainties presented in this paper are standard uncertainties.

Our reported vapor pressure values are related to our experimental measurements of fluorescence counts and temperatures through Eqs. (3) and (4)

$$p_Z = n_{Xe} \frac{C_Z^{K\eta}}{C_{Xe}^{K\alpha}} \frac{\sigma_{Xe}^K(E_i)}{\sigma_Z^K(E_i)} \frac{Y_{Xe}^K}{Y_Z^K} \frac{B_{Xe}^{K\alpha}}{B_Z^{K\eta}} \frac{\tau(E_{Xe}^{K\alpha})}{\tau(E_Z^{K\eta})} \frac{Q_d(E_{Xe}^{K\alpha})}{Q_d(E_Z^{K\eta})} kT. \quad (12)$$

The most important aspect of this relationship is that all but two factors appear as ratios of values of the same parameter. Ratios of the same parameter are much less susceptible to systematic errors. On the other hand, systematic errors in the Xe density in each cell n_{Xe} and the temperature T map directly into systematic uncertainties in the reported vapor pressures.

The uncertainties in n_{Xe} for each cell are given in Table I and are in the range of 6% to 9%. The uncertainty in our calibrating density in previous work was 13%.³ The improvements are due primarily to our improved method for comparing fluorescence intensities from different cells. That method is described in Section II.

The use of Xe as an internal standard of calibration rather than a substitution standard has provided the greatest improvement in our measurement precision. The improvement occurs in the ratio of counts $C_Z^{K\eta}/C_{Xe}^{K\alpha}$ where the two count values are now acquired simultaneously. Previously, the two count values were determined from different cells at different temperatures and this lead to uncertainties estimated to be 20% because of difficulty in maintaining a fixed position for the vapors cells and associated tantalum jacket.³ The internal standard completely eliminates those problems. The uncertainty in the ratio of counts is now dominated by statistical sources such as count statistics and background noise due to scattered photons. These uncertainties range from $\pm 40\%$ for the lowest reported vapor pressures to less than $\pm 1\%$ for the largest values.

A negative consequence of using an internal standard is the presence of additional fluorescence lines in the acquired spectra. The Xe K_β lines overlap with the Ce K_α lines, forcing us to use the much weaker Ce K_β lines to determine the Ce density. The I K_α and Xe K_α lines do not directly overlap, but lie very close to each other. In an effort to keep them fully resolved, we utilized a longer shaping time on the detector.

This had the effect of increasing the dead time of the detector, or equivalently reducing the number of fluorescence photons detected in a given integration time. This reduced the sensitivity of our present measurements by about an order of magnitude compared to our earlier work.³ Previously, we were able to measure pressures as low as about 10 Pa. Here, we were limited to pressures of 100 Pa and higher.

Uncertainties in cross sections σ , branching fractions B , and fluorescence yields Y are difficult to rigorously quantify. Gerward¹³ discusses errors in cross sections based on comparisons between experimental and theoretical values. For K-edge absorption by heavier atoms, data values are typically in agreement to within 1%. Exceptions are for energies within 1.5 keV of an absorption edge, for which errors are estimated at 10%. The higher uncertainty applies only to our measurements of Tl.

The comprehensive study of fluorescence yields by Krause¹⁴ gives uncertainties of 2% or less for the fluorescence yields used in our analysis. As values for fluorescence yields are obtained by a least-squares fit to experimental data, errors in these values are likely systematic across similar values of Z , and are thus generally reduced further in the ratio appearing in Eq. (12).

Rao *et al.*'s plot of experimental and theoretical values for the ratio of K_β to K_α fluorescence intensities as a function of Z speaks to the uncertainty in the ratios of branching fractions.¹⁵ Their comparison of published experimental and theoretical data implies that a ratio $B^{K\alpha}/B^{K\beta}$ has a random uncertainty of about 3%. (This case applies to our determination of vapor pressures corresponding to the total densities of Ce.) It also implies that ratios of K_α branching fractions have a much lower uncertainty. (This case applies to our analysis of all other elements.)

We estimate the combined uncertainty arising from cross sections, branching fractions, and fluorescence yields to be 3% for all cases except Tl, for which the combined uncertainty is 10%.

Ratios of the transmission values, though they are computed from absorption cross sections, do not reduce systematic uncertainties in quite the same way because of the nonlinear relationship between τ and the wall density, absorption cross section, and wall thickness. However, when τ is relatively high, as it is here, it is not so sensitive to these parameters. The smallest transmission value used in this work is $\tau = 0.65$ for the In K_α line through PCA. In this case, the relative uncertainty in τ is less than half the relative uncertainty in the product of the wall density, absorption cross section, and wall thickness. We estimate the uncertainty in the ratio of transmission factors to be 10%.

The quantum efficiency Q_d of a detector can be difficult to measure on an absolute scale. Fortunately, only relative values for the quantum efficiency are needed here. Furthermore, Q_d does not change significantly over the range of interest (20 keV to 75 keV) for the detector we used and for the geometry of our experiment. Thus, we assume that the quantum efficiency is the same in all cases, an assumption that is probably accurate to within 1%.

The dominant source of uncertainties in our temperature measurements arises from spatial variations in temperature.

The strongest evidence for the magnitude of these uncertainties are the differences in temperatures measured by the two thermocouples (Figure 4). These differences were in the range of 1.5 K to 5.5 K, with the larger differences occurring at $T = 1400$ K. Various tests indicated that these temperature differences are real and probably originate in asymmetries in the custom-built oven, including uneven N_2 purge flows. The point in the vapor where our fluorescence measurement occurs may not be at the same temperature as the cold spot in the cell, where the salt condensate presumably lies. The former may be the hottest spot in the oven and may be hotter than either thermocouple. But the latter, because of the exponential dependence of equilibrium constants on temperature, is probably more significant. We average the values from the two thermocouples and estimate the uncertainty in our reported temperatures as ± 4 K at $T = 900$ K and ± 8 K at $T = 1400$ K, with a linear extrapolation in between these two temperatures. A temperature change of $\Delta T = 8$ K at $T = 1400$ K corresponds to $\Delta P/P \approx 0.1$ for the vapor pressure corresponding to the total density of Ce in the vapor over pure CeI_3 .

The free energies of formation used in the thermochemical calculations and given in Table II cannot be considered measured values. The specified species and free energy values are both mathematically possible and mathematically simple solutions to the problem of matching calculations to observed measurements. They are undoubtedly not unique, and may not even be physically realistic solutions, at least as far as the temperature dependence of the free energies are concerned. There are still lingering discrepancies, although modest, especially with I, as already noted. Furthermore, most of the free energy of formation values proposed here are dependent on other published free energy values or equilibrium constants whose uncertainties have generally not been adequately tested. The values in Table II are instead given so that the modeling results can be reproduced if desired.

As has been noted with almost every system studied in this work and in Ref. 16, the observations of I continue to reflect anomalous behavior. In cell C14, the I content is about 50% larger than the Tl content across all temperatures where we would expect them to be equal based on the 1:1 stoichiometric ratio in TII. At the highest temperatures the I content grows a little faster than the Tl content as the evaporation of CeI_3 begins to become significant. In cell C15, the I content is only about 10% larger than Tl across most of the temperature range. At the lowest temperatures, the larger difference may be due to water contamination. The I content, and the reactions underlying it, appear to be more complex than previously imagined. The observed anomalies do not appear to be related to measurement uncertainties.

The salt doses in the cells have likely differed from their target values. Variations in a minority salt make a difference in the performance of the system. This does not affect the accuracy of our measurements, but it does add uncertainty about what system we are measuring. It is essential to have a reliable method for measuring the salt doses in the vapor cells and for verifying the purity of these doses.

V. CONCLUSION

We used x-ray induced fluorescence to study the vapors in equilibrium with pure CeI_3 , as well as CeI_3 mixed with high and low molar ratios of the Group 13 metal-iodides GaI_3 , InI , and TlI . Measurements of vapor pressures corresponding to the total densities of Ce, In, Tl, and I were obtained over the temperature range 900 K to 1400 K. The measurements of Ce had acceptable signal-to-noise ratios only for temperatures exceeding the melting point of pure CeI_3 , $T \approx 1033$ K. These measurements showed enhancement of Ce in the presence of InI and TlI , but not GaI_3 . Enhancement was strongest at lower temperatures. Equilibrium thermo-chemical modeling indicates the importance of both liquid- and vapor-phase complexes in the CeI_3/InI and CeI_3/TlI systems.

The uncertainties in the measured vapor pressures were greatly reduced from previous work by using an internal calibration in the form of Xe in the salt-filled cells. Standard uncertainties excluding measurement signal-to-noise are estimated to be $\pm 17\%$ for all cases except Tl, which is $\pm 20\%$. Standard uncertainties in individual data points from measurement noise range from $\pm 40\%$ to less than 1%.

The value of the measurements would be greatly enhanced by better knowledge of the salt doses. Our simulations indicate significant deviations from the target values for some of the minor salts.

We continued to see, as in previous work, significant and varied anomalies in the the I content of the vapors. These anomalies are unexplained by numerical simulations.

ACKNOWLEDGMENTS

Use of the Advanced Photon Source was supported by the U. S. Department of Energy, Office of Science, Office of Basic Energy Sciences, under Contract No. DE-AC02-06CH11357. We thank Ali Mashayekhi and Roger Ranay of the Advanced Photon Source for their help on the beamline; Nick Guise of NIST for computer programming; and Joanne Browne, Victor Perez, Jeff Neil, Michael Quilici, and John Kelso of OSRAM SYLVANIA, Inc., for cell preparation;

¹S. Boghosian and G. N. Papatheodorou, in *Handbook on the Physics and Chemistry of Rare-Earths* edited by K. A. Gschneidner, Jr. and L. Eyring (Elsevier Science, Amsterdam, 1996), Vol. 23, Chap. 157, p. 435.

²R. Lorenz, *Lighting Res. Technol.* **8**, 136 (1976).

³J. J. Curry, A. Henins, W. P. Lapatovich, E. G. Estupiñán, S. D. Shastri, and J. E. Hardis, *J. Chem. Phys.* **139**, 124310 (2013).

⁴J. J. Curry, W. P. Lapatovich, and A. Henins, in *Advances in Atomic, Molecular, and Optical Physics* edited by E. Arimondo, P. Berman, and C. C. Lin (Academic Press, San Diego, 2011), Vol. 60, Chap. 2.

⁵S. D. Shastri, K. Fezzaa, A. Mashayekhi, W.-K. Lee, P. B. Fernandez, and P. L. Lee, *J. Synchrotron Radiat.* **9**, 317 (2002).

⁶M. J. Berger, J. H. Hubbell, S. M. Seltzer, J. Chang, J. S. Coursey, R. Sukumar, D. S. Zucker, and K. Olsen, *Xcom: Photon cross sections database, nist standard reference database 8*, see <http://www.nist.gov/pml/data/xcom/index.cfm> (1998).

⁷D. R. Cruise, *J. Phys. Chem.* **68**, 3797 (1964).

⁸*NIST-JANAF Thermochemical Tables*, edited by J. M. W. Chase, 4th ed. (American Chemical Society and American Institute of Physics, Woodbury, NY, 1998).

- ⁹*Thermochemical Data of Pure Substances*, edited by I. Barin, 2nd ed. (Verlagsgesellschaft mbH, New York, 1993), in collaboration with F. Sauert, E. Schultze-Rhonhof, and W. S. Sheng.
- ¹⁰S. Hansen, R. Steward, J. Getchius, and T. Brumleve, *Supplement to Vapor Pressure of Metal Bromides and Iodides* (APL Engineered Materials, Inc., Urbana, Illinois, 2000).
- ¹¹M. Ohnesorge, Ph.D. thesis, Forschungszentrum Jülich (2005).
- ¹²C. S. Liu and R. J. Zollweg, *J. Chem. Phys.* **60**, 2384 (1974).
- ¹³L. Gerward, *Radiat. Phys. Chem.* **41**, 783 (1993).
- ¹⁴M. O. Krause, *J. Phys. Chem. Ref. Data* **8**, 307 (1979).
- ¹⁵P. V. Rao, M. H. Chen, and B. Crasemann, *Phys. Rev. A* **5**, 997 (1972).
- ¹⁶J. J. Curry, E. G. Estupiñán, A. Henins, W. P. Lapatovich, S. D. Shastri, and J. E. Hardis, *Appl. Phys. Lett.* **100**, 083505 (2012).
- ¹⁷PCA is commonly used to make the arc tubes of metal-halide high-intensity discharge lamps.
- ¹⁸Xe is well-suited for calibration because its density does not depend on temperature and its fluorescence energy is similar to the elements being observed.
- ¹⁹Fluorescence from elements lighter than Kr occurs at energies too low to be transmitted by the cell. The beam energy of 61 keV used for measuring cells C17 and Q4 was too low to excite K-shell fluorescence in elements heavier than Tm.